Inland Water Body Mapping Using Multitemporal Sentinel-1 SAR Data

David Marzi ⓘ, *Student Member, IEEE*, and Paolo Gamba ⓘ, *Fellow, IEEE*

Abstract—Climate change studies require increasingly detailed information on land cover and land use, to precisely model and predict climate based on their status and changes. A fundamental land cover type that needs to be constantly monitored by the climate change community is water, but currently there is a lack of high-resolution water body maps at the global scale. In this article, we present a fully automated procedure for the extraction of fine spatial resolution (10 m) inland water land cover maps for any region of the Earth by means of a relatively simple *k*-means clustering model applied to multitemporal features extracted from Sentinel-1 SAR sequences. Indeed, due to heavy cloud coverage conditions in many locations, multispectral sensors are not suitable for global water body mapping. For this reason, in this work, we deal only with SAR data, and specifically with multitemporal Sentinel-1 data sequences. The experimental results, obtained for three geographical areas selected because of their wide diversity in terms of geomorphology and climate, show an almost complete consistency with existing datasets, and improve them thanks to their finer spatial details.

Index Terms—Climate change, *k*-means, Sentinel-1, synthetic aperture radar (SAR), time series analysis, water mapping.

I. INTRODUCTION

IN THE context of climate change studies, there exist great interest in mapping and monitoring land cover (LC) types and their changes at the global scale [1], [2]. Indeed, it is necessary to produce high-resolution (HR) LC maps for consecutive years in order to better observe and analyze changes in terms of extent and/or transition of the classes, thus characterizing the effects of climate change from the local to the global scale. The most useful maps for LC types of interest at the global scale for climate change initiatives (CCIs) and their connection with Earth observation (EO) sensors have been provided by projects funded by the European Space Agency (ESA) CCI [3].

To obtain these maps, data from multiple satellite sensors have been employed, namely multispectral, hyperspectral, and microwave passive radiometers, as well as lidar and radar active sensors. Since each source of data has its own pros and cons, it is not possible to reliably map all classes with a single type of data.

For instance, optical systems (multispectral and hyperspectral sensors) are suitable to recognize surface materials by measuring their reflectance at different wavelengths, typically ranging from the visible to the infrared. For this reasons, optical data are widely used in vegetation mapping, agricultural applications, and soil characterization [4]. Due to its typical spectral signature, water is also well-distinguishable in optical data, and several water indices have been designed to detect water bodies by means of optical data, such as the normalized difference vegetation index, normalized difference water index (NDWI) [5], modified NDWI [6], and the automated water extraction index [7]. Still, constant monitoring of any LC type using optical sensors is a really challenging task in cloudy areas.

Thanks to the efforts of many researchers and the use of multispectral and radar datasets, several projects aimed at producing water body maps at the global scale were developed. These products (sorted by increasingly coarser spatial resolution) are summarized in Table I and subdivided in datasets dedicated only to water class and datasets that contain multiple information on different classes of water surfaces. The water and wetness product [8] from the European Commission Copernicus project is generated based on the fusion of multitemporal optical satellite imagery and synthetic aperture radar (SAR) data, and represents a thematic product that shows water occurrence from 2009 to 2018. The Landsat Dynamic Surface Water Extent (DSWE) [9] is a multiband raster layer representing per-pixel surface water inundation. The JRC Global Surface Water Mapping Layers [10] dataset contains maps of the location and persistence of surface water over the last 35 years, also providing statistics on the extent and change of those water surfaces. The Global Surface Water Dynamics product [11] highlights estimates of open surface water extent and change from 1999 to 2020. the Global WaterPack [12] is a 250-m resolution dataset revealing dynamics of global inland water bodies on a daily basis and represents the surface water map product having the highest temporal resolution with respect to all other products of Table I. The Global Forest Change Water Cover (GFCC30WC) [13] dataset provides surface-water information and was derived from water bodies' data mask in the GFCC Tree Cover (GFCC30TC) and Forest Cover Change (GFCC30FCC) products based on a classification-tree model. The Copernicus Global Land Service (CGLS) [14] delivers a global LC map that includes many classes, including water surfaces. Finally, the GlobCover Land Cover maps by the ESA CCI project [3] provide global annual LC maps and, contrary to all other LC types, water bodies are mapped with the Envisat advanced SAR (ASAR).

TABLE I
AVAILABLE GLOBAL WATER SURFACE PRODUCTS SUBDIVIDED IN TWO GROUPS AND SORTED BY INCREASINGLY COARSER SPATIAL RESOLUTION: THE FIRST GROUP RELATES TO PROJECTS, FOCUSING ONLY ON WATER BODIES EXTRACTION, WHEREAS THE SECOND GROUP IS DEVOTED TO PROJECTS AIMED AT GENERIC LC MAPPING

Data set	EO sensor(s)	Spatial res.	Ref. year(s)
Copernicus Land Monitoring Service – High Resolution Layer Water and Wetness (v2) [8]	Landsat-5, -6, -7 and -8, Sentinel-1A, ENVISAT-ASAR)	20 m	2009 - 2018
Landsat Dynamic Surface Water Extent (DSWE) [9]	Landsat-4, -5, -7, -8	30 m	1982 - present (2021)
JRC Global Surface Water Mapping Layers (v1.3) [10]	Landsat-5, -7, -8	30 m	1984 - present (2021)
Global surface water dynamics [11]	Landsat-5, -7, -8	30 m	1999 - 2020
Global WaterPack [12]	MODIS Terra & Aqua	250 m	2013 - 2015
Global Forest Cover Change Water Cover (GFCC30WC) [13]	Landsat-7, MODIS	30 m	2000
Copernicus Global Land Cover Layers (CGLS-LC100 collection 3) [14]	PROBA-V	100 m	2015 - 2019
GlobCover Land Cover Maps [3]	MERIS, Envisat-ASAR	300 m	1992 - 2018

The global surface products listed in Table I provide different information, such as permanent water bodies, maximum water extent, temporary water bodies, and change in time of water LC. The proposed procedure is able to extract water bodies that are permanent on any temporal interval, from one month to one or more years, exploiting Sentinel-1 data sequences. In this article, we focus on the extraction of annual maps of water bodies, following the requirements by the funding project.

Almost all the datasets listed in Table I are derived from multispectral sensors; on the other hand, SAR systems are not usually employed for generic LC mapping. Instead, they have proved to perform particularly well for peculiar LC types, such as built-up areas and water bodies [15], [16]. This is due to their sensitivity to physical and electromagnetic properties of the targets. In addition, because of their operating frequency in the microwave band, SAR signals can penetrate the atmosphere in any kind of weather conditions and, since SAR is an active sensor, they can also be acquired during night time. Thanks to these two properties, SAR sensors guarantee the acquisition of equally spaced temporal sequences.

Previous works proposed methodologies for water body extraction using SAR data by means of supervised classifications [17], thresholding techniques using quad-pol data [18], SAR and optical data fusion [19], and signature analysis in the feature space [20], [21].

In addition, Ferrentino *et al.* [21] demonstrated that the joint use of Sentinel-1 time series data and a metric based on the product of co- and cross-polarized channels can lead to an efficient support of the so-called "smart water management"; in particular, the proposed methodology, based on two steps, allows us to efficiently extract waterlines and retrieve water surfaces.

The study in [22] compares ten different feature combinations to train a supervised support vector machine model. The conclusion of the study states that optical indices are not useful as expected, and, from the accuracy point of view, the best SAR configuration for detecting water is the single-channel VH-polarized intensity data, with an average overall accuracy (OA) of 98.07%.

Finally, another interesting study is reported in [23], where a k-means clustering approach is employed with a number of extracted clusters $k = 15$. The methodology extracts features starting from a yearly Sentinel-1 time series obtained by averaging ascending and descending orbit images separately within each month (ending up with 12 two-average-composites per year), and VV and VH intensity data are used as inputs. Eventually, the temporal average backscatter value is computed for each cluster, and a specific threshold is applied to obtain the "water" class. Compared to the methodology proposed in this article, the work in [23] lacks the flexibility to be applied to other regions of interest because it does not exploit any initial set of water points. Moreover, the parameters are tailored to the specific area of interest.

All in all, the studies in technical literature have limitations, related to lack of automatism (e.g., manual sampling of training samples), the impossibility to apply the methodologies to other study regions without *a priori* information (e.g., because they have thresholds and decision steps calibrated for specific regions of interest), the high computational cost of working on quad-pol images, or the reduced classification capability over cloudy regions when optical data are employed. Moreover, the main characteristics of the global water products listed in Table I suggest that the limitations of those datasets are mostly related to the spatial resolution, which is coarser than the result obtainable with the proposed approach. Finally, almost no products use the great potential in terms of both spatial and temporal resolution of Sentinel-1 data.

Given all the abovementioned considerations, the objective of this work is to use datasets that have never been used to generate annual water surfaces maps with an unprecedented spatial resolution.

In this article, a novel fully automated water surface mapping algorithm is presented, able to deal with any region of the world, with no limitation in size and no prior information about the area. This is possible, thanks to the use of Sentinel-1 SAR data sequences, and the exploitation of previous medium-resolution (MR) global LC maps for an initial training sample collection. The entire, fully automated procedure has been implemented in Google Earth Engine (GEE) [24], a powerful "big data" cloud platform for remote sensing, global-scale geospatial analysis.

II. PROPOSED METHODOLOGY

The proposed unsupervised water body extraction processing chain is summarized in Fig. 1, and is meant to be applied to a
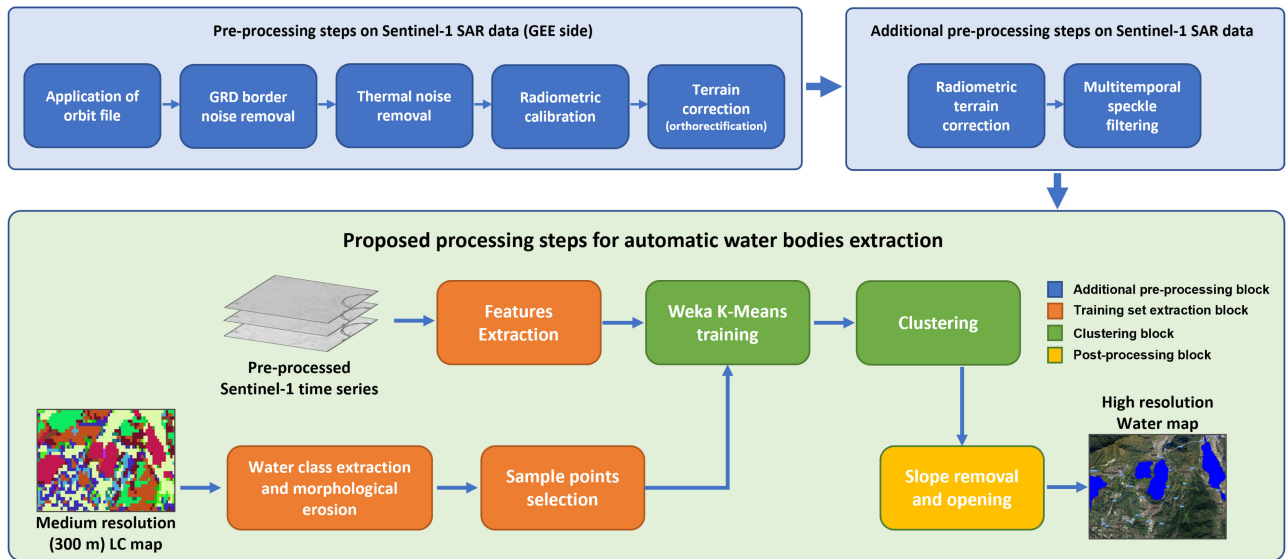
Fig. 1. Overview of the complete procedure designed to extract water bodies from Sentinel-1 SAR data sequences.

stack of multitemporal SAR data. First, a multitemporal denoising step is performed on the sequence of all the ascending and descending SAR images overlapping (completely or partially) the selected tile, aiming at reducing the effect of speckle noise. Then, a set of statistical and temporal features are computed to guide the k-means clustering algorithm. Finally, a few postprocessing steps (such as morphological operations and steep-slope removal) are applied to the classified result to improve the final water surface mapping accuracy.

A. Preprocessing

Before actual use, all the data must undergo several preprocessing steps. These steps, shown in Fig. 1, include the application of orbit file, GRD border noise removal, thermal noise removal, radiometric calibration, and terrain correction (orthorectification) using SRTM30 or ASTER DEM for regions located at more than $60°$ latitude, and are directly applied by the GEE cloud computing platform. Since the standard Sentinel-1 preprocessing chain does not include radiometric terrain correction, we added an angular-based radiometric slope correction routine for Sentinel-1 SAR images, developed in [25]. The idea behind such correction is to exploit an established physical reference model, which is also extended to simultaneously generate masks of invalid data represented by active layover. The radiometrically corrected SAR products significantly improve LC mapping on a large scale, especially over morphologically complex regions (e.g., mountains).

Moreover, our procedure adds a multitemporal speckle noise filter, applied to the sequence of Sentinel-1 SAR images according to [26]. The filtering algorithm starts with the estimation of a "super-image" obtained by averaging all the SAR images of the multitemporal stack. Then, the ratio between each original and noisy image and the super-image is computed; the result of this ratio is denoised with a 7×7 low-pass filter kernel; finally, each low-pass-filtered image is remultiplied by the super-image.

B. Feature Extraction

In this work, we rely only on the VH intensity data that proved to be the best selection in terms of classification accuracy in [22]. More specifically, the following VH-based temporal features are computed on a per-pixel basis from the denoised SAR time series: three-month composites, labeled "quarter composites" because they are obtained by averaging in time all the available SAR images within a temporal window roughly corresponding to a quarter of a year, as well as the annual mean, minimum, maximum, and variance. Variance and minimum are essential features when water mapping is the task; as a matter of fact, contrary to other LC types, water bodies are characterized by high temporal variability and very low minimum backscatter along the year [20].

The main difference between this approach and the one in [20] is the use of the so-called quarter composites, a possibility due to the low revisit time of Sentinel-1 constellation. Quarter composites help to better discriminate between water and similar classes. For instance, many agricultural fields are flooded several times along the corresponding crop growth season; therefore, their annual mean, minimum backscatter, and temporal variability parameters may be very close to those of water bodies. The selected four composites allow us to recognize the temporal pattern along the year due to the variability of specific LC types (e.g., because of the phenology in case of vegetation). Indeed, differently from a water body, agricultural fields will show significant phenological variations along the year, and this helps the classifier to recognize such fields as nonwater. Such discrimination may be more difficult if only annual (or multiannual) values are used, as in [20].

C. Training the k-Means Model

The abovementioned features are extracted first on a balanced HR set of *water* and *nonwater* points extracted from coarse maps, such as the MR GlobCover map. To this aim, first a binary mask

from the coarse map of water bodies is extracted and eroded with a 3×3 sliding kernel to increase the likelihood of sampling "pure" water pixels. In this case, the erosion procedure ends up with no water pixels in the considered tile, the original (not eroded) mask is restored and used for sampling. Whereas, if the tile of interest contains no water pixels in the MR map, an empty image (all zeroes) is provided in output. To sequentially extract a map all over the world, the Sentinel-2 tile system is used [27], and $\approx$ 10.000 km^2, i.e., 100 million pixels at 10-m resolution, are analyzed at a time. Finally, a stratified random sampling is applied to the binary mask to generate up to 1000 points over water regions and 3000 points over nonwater regions.

These training points are used as initial seeds for the k-means clustering algorithm, and the model extracted from them is eventually used to cluster all points belonging to the area of interest. Note that the k-means algorithm implemented in GEE is based on the "Weka" open-source machine learning software [28], optimized to work with large datasets. Starting from a representative subset of the data (the abovementioned HR training set), the Weka k-means algorithms generate a model that is then used to make predictions on the full dataset.

Even if it may look counter-intuitive, the k-means algorithm is run with $k = 4$; this means that each training pixel is automatically assigned to one among four classes. The number of classes comes from the idea that inside the initial mask there may be water, vegetation, bare, or impervious soil. Indeed, we experimentally found that the use of $k = 2$ clusters leads in many cases to confusion between water and some of these classes. By increasing k, the k-means model performs a more reliable clustering since the potentially confusing classes are clustered in different nonwater clusters. This results in a more robust discrimination of water bodies from the other LC types, and drastically reduces the number of false positives. Since k-means makes no assumptions on the distribution of the data, it is a suitable approach to deal with multitemporal SAR composites, whose statistical characteristics are very complex.

In addition to the rather simple algorithm described in the previous paragraphs, and in order to avoid oversampling the water class when the tile include wide open water areas (such as portions of seas and oceans), the shoreline/coastline data from the Global Self-consistent, Hierarchical, High-resolution Geography Database (GSHHG) is used to mask out open water from all Sentinel-1 images [29] before the clustering is applied. GSHHG is a free, HR geography dataset containing the "World Vector Shorelines," a shapefile of the shorelines of the entire Earth, available at different spatial resolutions. For this work, the "high resolution" shapefile is used, obtained by using the Douglas–Peucker lines-reduction algorithm to reduce the maximum number of vertices of the "full resolution" shapefile by 80%.

D. Automatic Water Cluster Extraction

Once four clusters have been extracted, a simple yet effective method is applied to automatically select the one representing the water class. To this aim, the original water mask derived from the CCI LC map is converted from raster to vectors. Then, a negative buffer of 100 m is applied to the vectorized water mask and a frequency histogram is computed over the four-cluster

result, within the multipolygon boundaries. Since the frequency histogram shows frequencies for each cluster, i.e., how many times each cluster occurs inside the vector layer, we assumed the cluster associated with highest frequency to be representative of the water class. Such cluster is eventually extracted as the final HR water map.

E. Postprocessing of the Clustering Result

The final HR water map eventually undergoes a few postprocessing steps to get rid of isolated pixels and residual false positives.

The radiometric terrain correction preprocessing step allows us to correct for slope-induced backscatter differences, which are mainly caused by hills and mountains due to the natural slanted acquisition geometry of SAR systems.

Notwithstanding the great effectiveness of the radiometric terrain correction in reducing the backscatter dependency to the terrain geometry, the approach used in this work is a simplified angular-based model and presents some limitations, which translate into residual topographic effects. These effects are mainly related to the inaccuracy of the used DEM, the assumption of homomorphism between map (geocoded imagery) and radar geometry, and the image geometry approximations [25]. Moreover, unlike the radiometric terrain correction model chosen for this work, pixel-area-based slope correction models—which account for actual topology between map and radar geometry—are proven to be more accurate and suitable to address this issue [30]. However, such algorithms are impractical to use within GEE, since the area of the pixel should be computed on the fly, causing long run-times and/or memory saturation issues.

Due to the abovementioned residual topographic effects, false positive occurrences may persist over steep-sloped regions. A simple slope masking proved to be enough to get rid of the remaining false positives over these regions. To this aim, a steep-slope masking using the ALOS World 3D - 30 m [31] digital surface model (DSM) from the JAXA Earth Observation Research Center is applied. The ALOS DSM is a globe-covering raster dataset where each pixel represents height above sea level at 30-m spatial resolution. To derive slopes from the elevation data, the local gradient is computed using the four-connected neighbors of each pixel. The resulting product was finally used to mask out terrain pixels with slope greater than 8°.

Lastly, an "opening" morphological operation with a 3×3 kernel is applied to the slope-filtered result. The effect of this operation is the removal of foreground (bright) pixels. Contrary to a simple erosion, which may be too disrupting, the opening operation is defined by an erosion followed by a dilation; therefore, at the cost of a slight loss of spatial details, the spatial resolution is 30×30 m^2, while the posting of the final result is 10 m.

III. STUDY AREAS

To prove its effectiveness, the proposed methodology has been applied to the following three regions with completely different geomorphology and climate, as shown in Fig. 2.

1) *Siberia (Sentinel-2 tile 42WXS, Fig. 2 top left):* This region is characterized by many complex rivers and water bodies
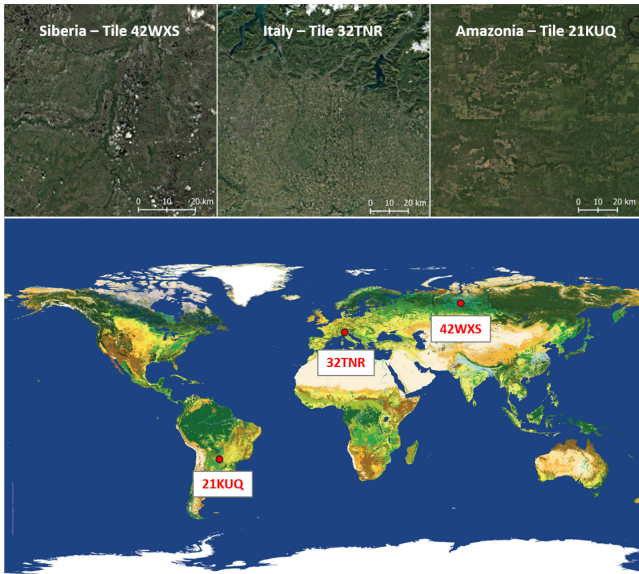
Fig. 2. Test regions. From left to right, the Google satellite basemap view of Siberia (tile 42WXS), Italy (tile 32TNR), and Amazon (tile 21KUQ). The bottom image is the visualization of the 2018 Medium Resolution Land Cover map from the ESA CCI project with the location of the three areas.

covered with ice and snow for 75% of the year. Extremely cold weather is dominant during the whole year, ranging from –40 to +20 °C. Here, the advantage of using multi-temporal SAR data is twofold: SAR signals can penetrate clouds and rain, ensuring periodic data acquisitions; moreover, since most water bodies tend to vanish during the cold seasons, time series of SAR images help the detection of such bodies thanks to their particular change in time.

2) *Amazon (tile 21KUQ, Fig. 2 top right):* This region is dominated by vegetation and hot, tropical weather. Over this region, it is very difficult to obtain cloud-free optical images due to such harsh climate. Temperature ranges from 22 to 40 °C, and the rainfall is persistent during most of the year, ranging from 200 to 320 mm every single month with an average of 89% of humidity.

3) *Northern Italy (the whole Lombardy region and the tile 32TNR, Fig. 2 top middle):* The climate in this tile is Mediterranean, with temperatures ranging from 20 to 33 °C during summer and from –1 to 10 °C in winter. Clouds, fog, and haze are often present, and the region includes a small minority of mountainous areas in the north that make it complex in terms of morphology.

As mentioned above, these three different study areas were selected to test the robustness and reliability of the proposed methodology in situations with very few common features.

On these areas, free data by the Sentinel-1 SAR constellation in the framework of the Copernicus program were used. The Sentinel-1 SAR antenna operates in the *C*-band with a central frequency of 5.405 GHz (roughly 5.5-cm wavelength) and is capable of providing a radiometric accuracy within 1 dB.

Regarding polarization modes, Sentinel-1 is able only to provide dual-pol images acquired with vertical transmit, vertical receive (VV) and vertical transmit, horizontal receive (VH) polarizations in different acquisition modes: stripmap, interferometric

wide swath (IW), extra-wide swath, and wave. In this work, the VH channel intensity from the IW acquisition mode is used. The acquisition incidence angle in the IW mode can range from 29.1° to 46° across the range direction and, even if the incidence angle variation heavily affects backscatter intensity, for water mapping applications this variation is not critical, due to the dominance of strong mirror reflection backscatter mechanism over flat areas. Moreover, since the data have been subject to radiometric terrain correction, incidence-angle-related effects are more attenuated.

The year considered in this study is 2019, and 27, 60, and 31 IW VH-polarized SAR images acquired over Siberia, Italy, and Amazon, respectively, were considered for the analysis. Note that the number of available images intersecting (even partially) the region is much larger; however, only images overlapping at least 70% of one of the test areas were considered.

IV. RESULTS AND DISCUSSION

In this section, a few qualitative and quantitative results are presented.

First, Fig. 3 shows the final classification results at 10-m spatial resolution over tiny areas inside the selected test regions compared with the GlobCover map (300-m spatial resolution). By visual comparison, it is clear that the water areas delineated in the MR maps are confirmed in the HR map extracted by the proposed approach. Moreover, in the latter, water pixels inside very small water bodies and narrow river branches are also extracted, while they are not visible in the other maps.

A more detailed, but still qualitative analysis, is shown in Fig. 4, where the analysis is enlarged to compare samples of the extracted maps with the abovementioned water layer of the GlobCover, but also the Copernicus Global LC map (100-m spatial resolution) and the JRC Global Surface Water Mapping Layer (30 m). A visual comparison confirms that using the proposed technique a map consistent with those available is obtained, with the potential to disclose more details due to the finer spatial resolution.

To quantitatively prove the consistency between the new result of this work and the existing maps, a random sample of the GlobCover/Copernicus/JRC maps was extracted and the extracted sampled pixels were compared with those of the 10-m water map. Specifically, up to 1000 pixels for both the *water* and *nonwater* classes were selected. The confusion matrices for the study cases with respect to each compared datasets are given in Table II. Note that before sampling the reference maps, they were eroded using a square kernel with radius of 50 m, in order to avoid pixels in transitional areas.

From the confusion matrices, the producer accuracy for both the *water* (PA_w) and *nonwater* (PA_{nw}) classes, and the OA values were computed as a way to evaluate the consistency between the maps obtained by the proposed technique and the reference maps. All the results are summarized in Table III. Even if these results do not provide a real validation, but only a comparison between the extracted water body maps and the preexisting and coarse resolution water maps, they are extremely promising since, on average, the OA is around 96.2% when the best water map in terms of spatial resolution, the JRC map, is adopted as reference.
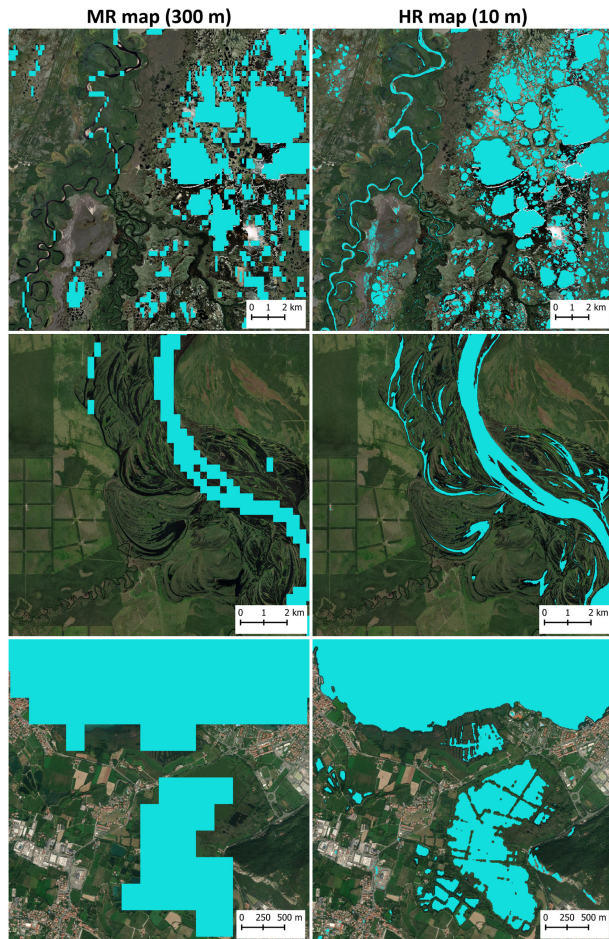
Fig. 3. Qualitative results over very small areas inside the considered tiles. The images on the left show samples from the 300-m spatial resolution water layer in the GlobCover map. The images on the right show instead the output of the proposed methodology with a spatial resolution of 10 m in Siberia (top), Amazon (middle), and Italy (bottom). In all the cases, water regions are colored in light blue and overlapped to the Google Satellite basemap.

A. Validation of the Proposed Method on the Lombardy Region

To accurately validate the proposed methodology, and provide a meaningful and reliable quantitative analysis of the final map, the water bodies for the whole Lombardy region in northern Italy were extracted. The region has an extent of 23.863 km^2 and is characterized by a large number of water bodies with different characteristics, such as big rivers with their tributaries and branches and numerous very large and small lakes of glacial origin. In addition, the morphology of the area is quite variable, from the main Po valley to hilly and Alpine mountainous areas.

All the described characteristics of the Lombardy region were considered challenging enough to test our methodology and provide an accurate validation analysis. Moreover, the whole area is covered by official land use data, provided by the Regional Territorial Information Infrastructure. In particular, we used the Destinazione d'Uso dei Suoli Agricoli e Forestali (DUSAF), Agricultural and Forestry Land Use, catalog of year 2018, a huge, detailed geographic database containing information on many different LC types [32]. In its latest version (DUSAF 6.0), a greater level of detail has been added thanks to the

TABLE II
Confusion Matrices for the Three Regions of Interest, Generated Based on Test Points Collected From the Three Different Reference Maps: The CCI GlobCover (300 M), the CGLS (100 M), and the JRC (30 M)

		Siberia this paper		Amazon this paper		Italy this paper	
		W	**NW**	**W**	**NW**	**W**	**NW**
CCI	**W**	805	194	205	84	840	160
	NW	45	955	8	966	1	993
CGLS	**W**	881	119	922	78	952	48
	NW	63	937	8	968	5	987
JRC	**W**	909	90	952	48	985	15
	NW	54	946	4	979	5	992

Notes: "W" and "NW" stand for water and nonwater, respectively.

TABLE III
OA, *Water* Producer Accuracy (PA$_w$), and *Nonwater* Producer Accuracy (PA$_{nw}$) for Each Study Case Using CCI GlobCover (300 M), the CGLS (100 M) and the JRC (30 M) Map as References

		Siberia	Amazon	Italy
CCI	PA_w	80.6	71	84
	PA_{nw}	95.5	99.2	99.4
	OA	88	92.7	91.9
CGLS	PA_w	88.1	92.2	95.2
	PA_{nw}	93.7	99.2	99.5
	OA	91	95.6	97.3
JRC	PA_w	91	95.2	98.5
	PA_{nw}	94.6	99.6	99.5
	OA	92.8	97.4	98.5

exploitation of very high spatial resolution SPOT6/7 satellite images (1 pixel = 1.5 m).

The DUSAF 6.0 LC legend is structured according to five hierarchic levels: the first three consist of the classes present in the Corine LC project [33], while the last two levels describe classes typical of the Lombardy region. The first level is in turn divided in five "fundamental" classes and, among these, the "water bodies" class.

Since the DUSAF 6.0 reference data have a spatial resolution of 1.5 m, it is necessary to make it compatible with the 10-m spatial resolution of the extracted map. To this aim, a negative buffer on the vector data representing the reference water bodies was applied. By doing so, two typologies of water bodies that cannot be detected by definition in Sentinel-1 SAR data were excluded from the validation experiment to avoid any negative bias. The first set is composed of very small water bodies with size less than one Sentinel-1 pixel, i.e., $\approx 100\,\mathrm{m}^2$. The second set is composed of long and thin water bodies, such as very narrow river branches with a width smaller than the spatial resolution of the SAR sensor.

Fig. 5 provides a visual comparison between the considered validation set and the map extracted in this work, generated by classifying nine 100×100 km^2 tiles. Starting from the validation set, a total of 20000 points, equally distributed between water and nonwater classes, were collected. All these points were
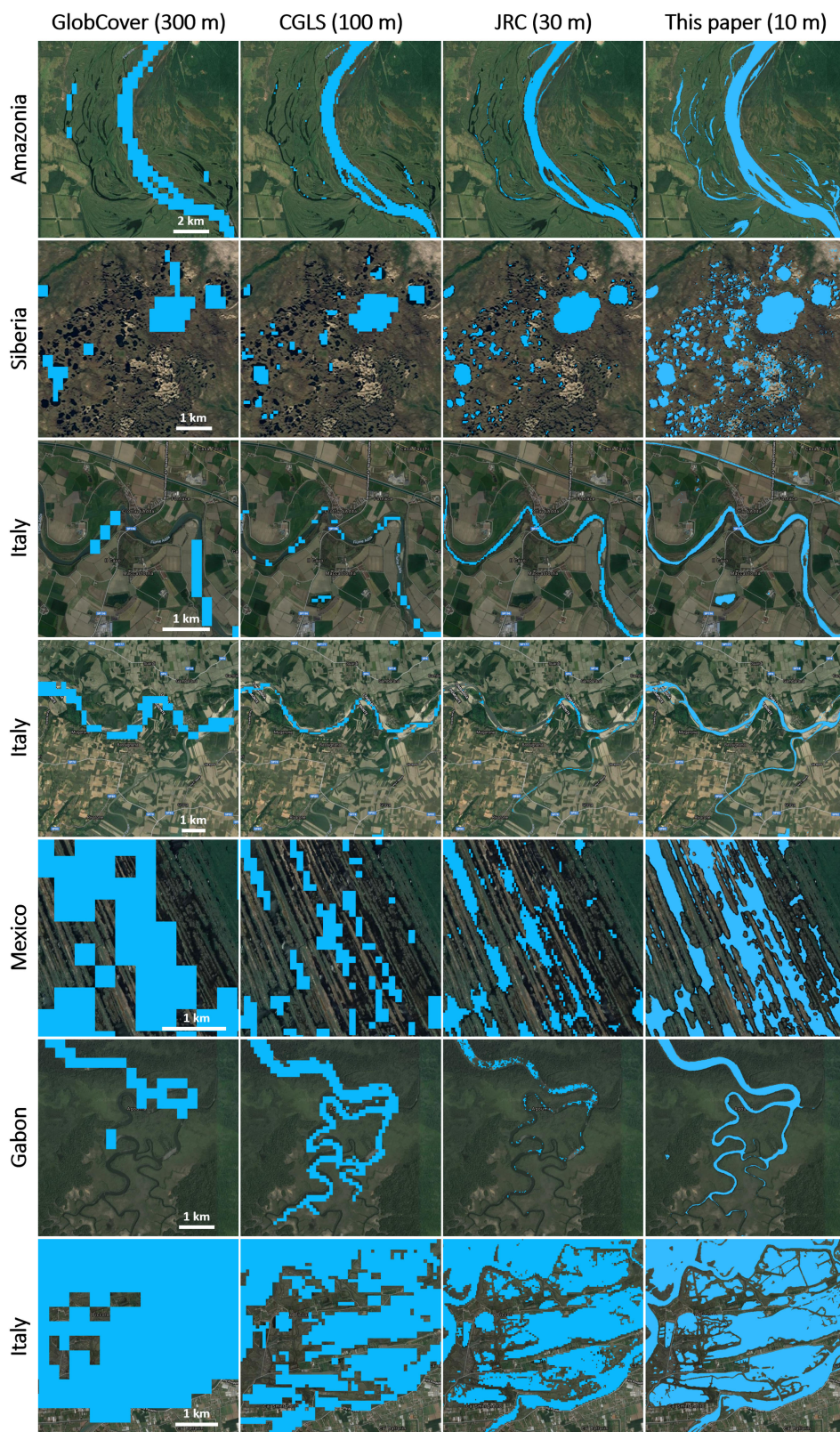
Fig. 4. From left to right, visual comparison among the water layer of the GlobCover (300-m spatial resolution) and the CGLS map (100 m), the JRC Global Surface Water Mapping Layer (30 m), and the results of the proposed approach (10 m). The considered zoomed areas are located in the Amazon (−22.728, −57.93142), Siberia (64.1333, 72.9079), Italy (45.161, 9.8607), Italy (45.0084, 8.7647), Mexico (22.0452, −105.5576), Gabon (0.0923, 9.6849), and Italy (45.4823, 12.5104). Background images are taken from the Google Satellite basemap, and the coordinates (latitude and longitude) are expressed in decimal degrees (WGS 84).
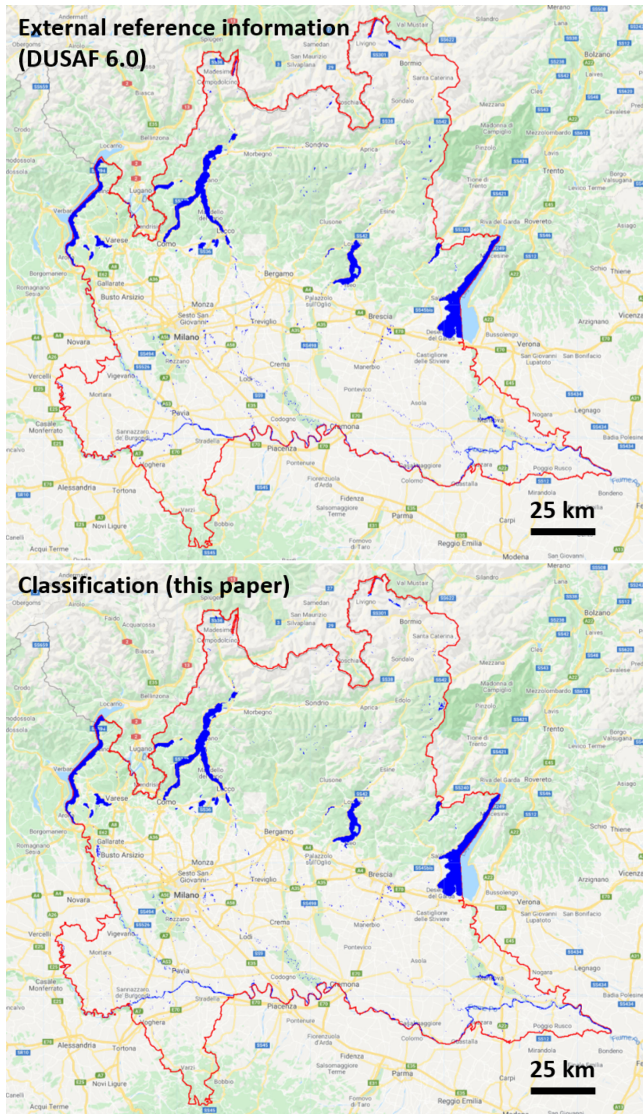
Fig. 5.   Visual comparison between the validation set (top) and the extracted water bodies map (bottom) for the whole Lombardy region. Both sets are presented in blue and superimposed on the Google Maps layer of the region.
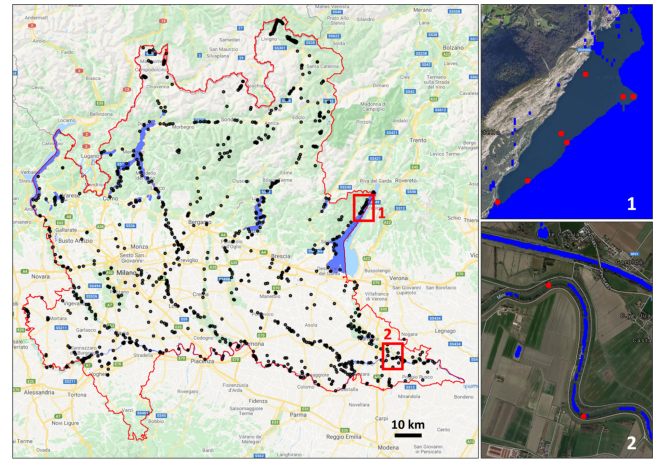

Fig. 6.   Spatial distribution of omitted water points for a specific classification run. Case 1: Foreshortening and layover. Case 2: Small water bodies not extracted or canceled by morphological operations. Omission points lay on the background image, which is represented by the Google Maps layer (over which the boundaries of the Lombardy region, in red, are superimposed).

then used to sample the classification result, build a confusion matrix, and compute the producer and OA. This process was repeated ten times by changing the random locations of the validation samples in order to prove the stability of the classification procedure.

The methodology achieves, on average, an OA of 94.6%, with a standard deviation of the order of 10^{-3}, meaning that the OA is not affected by the change of the location of the validation samples. The producer's accuracy is, on average, 89.4% and 99.8% for *water* and *nonwater* classes, respectively.

To further assess the limits of the proposed classification procedure, examples of omission occurrences for the water class were investigated. To this aim, a map highlighting all the points over which the proposed method fails to extract water bodies was built. On average, 9.3% of actual water class are not extracted by the proposed procedure. The spatial distribution of these points was thus analyzed to better understand under

which conditions the extraction fails. In Fig. 6, it is possible to observe the distribution of omitted water points in the region after classification.

There are two notable cases. The first one is due to the complex terrain morphology. Case 1 in Fig. 6 shows an example in a lake whose boundaries are characterized by steep and overhanging hilly banks. In such conditions, SAR images suffer from strong foreshortening and layover effects, the latter is dominant in this area.

The second source of omission errors, depicted in Case 2 of Fig. 6, is due to the presence of small and/or long and thin water bodies. In this case, such bodies are not extracted or they are classified as thin lines of pixels, which tend to disappear when applying the final opening step that was included to reduce false positives. Other cases of omission may also be represented by thin rivers surrounded by vegetation laying upon them.

B. ESA WorldWater Round Robin: An Additional Validation

In Fig. 7, a qualitative analysis carried out within the (ESA) WorldWater project round robin is reported [34]. The goal of the project was to enable a better understanding of the pros and cons of EO approaches for mapping and monitoring the extent of inland open waters, comparing the robustness of different algorithms and identifying shortfalls and areas of further research. Five challenging regions of the world, characterized by completely different climates and environments, were selected as test sites (characteristics of each area are shown in Fig. 7, together with their slope distributions shown in Fig. 8), and the participants were asked to produce monthly surface water maps, from July 2018 to June 2020, for each test site (120 water maps in total). The entire validation process was independently carried out by the project organizers using harmonized very HR (VHR) multispectral reference data from PlanetScope satellites (3-m spatial resolution). A total of 7.038 VHR reference points were used to validate the methodology (2.486 water points and 4.552
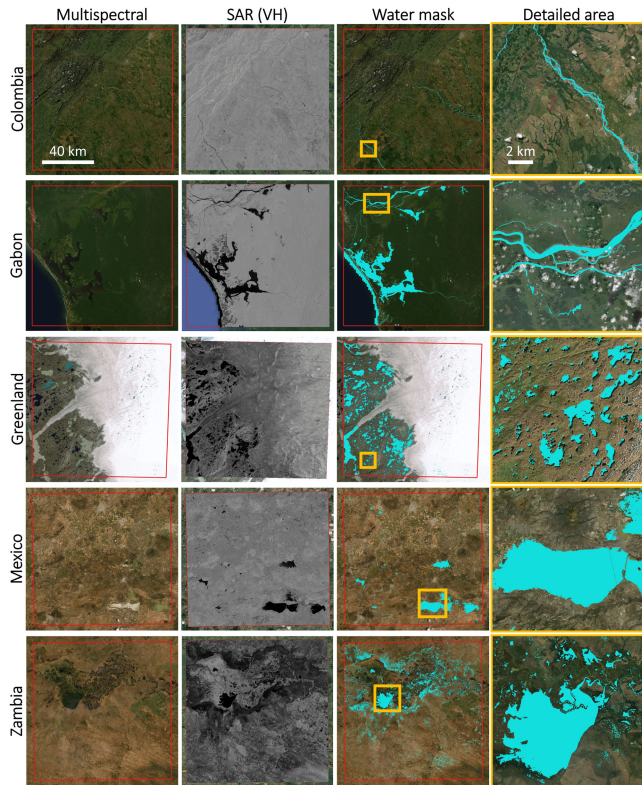
Fig. 7. Qualitative results for five critical test areas. A mountainous region with rivers and farmlands in Colombia (tile 18NYL); a complex lagoon system of rivers and lakes in Gabon (tile 32MND); a dense network of inland and supraglacial lakes in Greenland (tile 22WET); an inland dry forest region mixed with agricultural lands in Mexico (tile 14QKH); a region dominated by seasonally- and permanently flooded grasslands in Zambia (35LNC). Background optical images are taken from the Google Satellite basemap, except for the second column, which shows the annual mean VH composite image for each tile of interest (the grayscale composite is obtained by setting -30 and 0 dB for minimum—black—and maximum—white—σ^0 values, respectively). The scale bar is shown only once for full view of the tiles and for the detailed, zoomed region.

TABLE IV
RESULTS FROM THE ESA WORLDWATER PROJECT VALIDATION PROCESS. "W" AND "NW" STAND FOR WATER AND NONWATER, RESPECTIVELY, WHEREAS PA, UA, AND OA STAND FOR PRODUCER ACCURACY, USER ACCURACY, AND OA, RESPECTIVELY (IN PERCENTAGE [%])

	PA_w	PA_{nw}	UA_w	UA_{nw}	OA
Zambia	88	95	82	97	93
Mexico	83	99	98	91	93
Colombia	76	98	87	95	94
Gabon	98	98	99	96	98
Greenland	89	88	91	86	89
Average	86.8	95.6	91.4	93	93.4

nonwater points). As summarized in Table IV, the performances of our water extraction approach are very promising. The aim of such analysis is to provide evidence of the scientific robustness of the proposed methodology, by extracting water bodies in very diverse conditions.
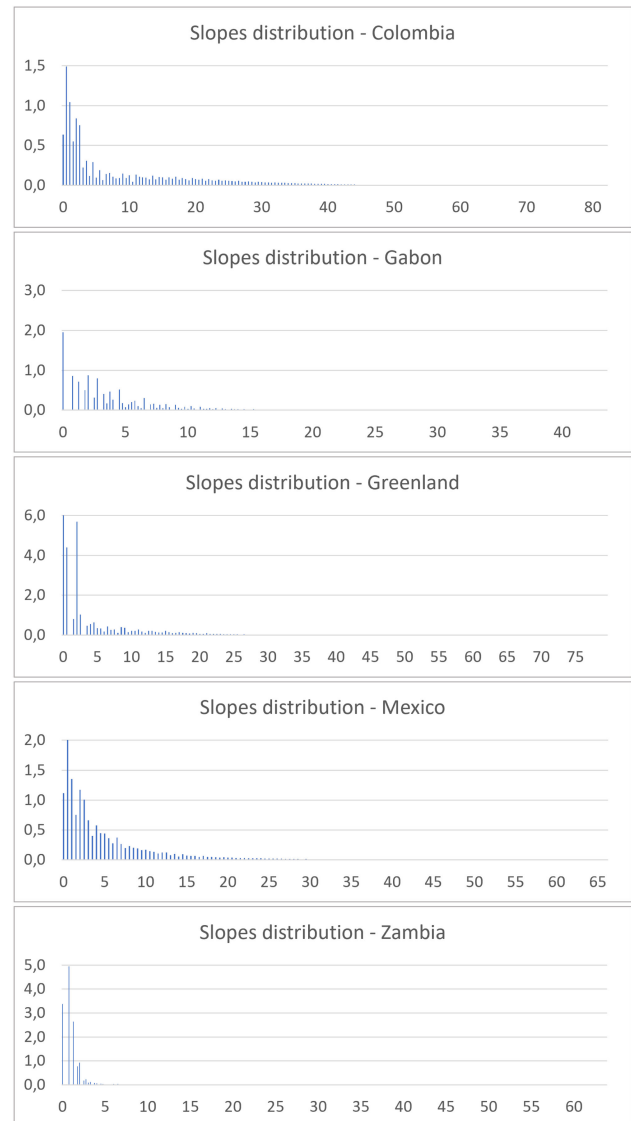

Fig. 8. Slopes distribution histogram of each round robin regions test site. Slopes in degrees [°] on the x-axis and frequency (in millions) on the y-axis.

V. CONCLUSION

This article presented an effective algorithm for water surface mapping using multitemporal HR Sentinel-1 SAR data. The proposed approach allows us to extract water bodies in a wide geographical area, automatically generating clustering seeds from preexisting coarser global water maps, such as the GlobCover LC map at 300-m spatial resolution. The use of multitemporal data enhances the capability to detect temporary water bodies (e.g., lakes covered by ice, snow, or vegetation during portions of the year), and also limits the effects of speckle noise. The use of a DSM increases the classification accuracy in morphologically complex regions by reducing false positives.

A thorough validation performed on the water body map for the whole Lombardy region (north of Italy), using external reference information provided by the regional mapping authority, certifies that the proposed automatic methodology achieves OA

values higher than 94%, with a slightly less good performance for water points than for nonwater classes (89.4% versus 99.8% producer accuracy, respectively). These results confirm the reliability of the proposed procedure, which has also been tested for consistency with similar global products. They also stress the robustness of the proposed extraction methodology on very wide areas, since nine 100×100 km^2 tiles (each corresponding to the size of a single, conventional Sentinel-2 tile) were processed to characterize the whole of Lombardy.

An additional validation test was also independently carried out by the ESA WorldWater organizers over five 100×100 km^2 test sites, using highly reliable VHR PlanetScope data. Notwithstanding the challenges represented by the diversities of the sites in terms of terrain complexity, climate, and water bodies types, our model was able to achieve, on average, 93.4% OA.

ACKNOWLEDGMENT

REFERENCES

[1] S. Bontemps *et al.*, "Consistent global land cover maps for climate modelling communities: Current achievements of the ESA's land cover CCI," in *Proc. ESA Living Planet Symp.*, 2013, pp. 9–13.

[2] R. Prestele *et al.*, "Current challenges of implementing anthropogenic land-use and land-cover change in models contributing to climate change assessments," *Earth Syst. Dyn.*, vol. 8, no. 2, pp. 369–386, 2017.

[3] ESA, *Cover CCI Product User Guide Version 2.* Tech. Rep., 2017, Accessed: Nov. 24, 2021. [Online]. Available: maps.elie.ucl.ac.be/CCI/viewer/download/ESACCI-LC-Ph2-PUGv2_2.0.pdf

[4] J. Transon, R. d'Andrimont, A. Maugnard, and P. Defourny, "Survey of hyperspectral earth observation applications from space in the Sentinel-2 context," *Remote Sens.*, vol. 10, no. 2, 2018, Art. no. 157.

[5] S. K. McFeeters, "The use of the normalized difference water index (NDWI) in the delineation of open water features," *Int. J. Remote Sens.*, vol. 17, no. 7, pp. 1425–1432, 1996.

[6] H. Xu, "Modification of normalised difference water index (NDWI) to enhance open water features in remotely sensed imagery," *Int. J. Remote Sens.*, vol. 27, no. 14, pp. 3025–3033, 2006.

[7] G. L. Feyisa, H. Meilby, R. Fensholt, and S. R. Proud, "Automated water extraction index: A new technique for surface water mapping using landsat imagery," *Remote Sens. Environ.*, vol. 140, pp. 23–35, 2014.

[8] Copernicus Land Monitoring Service, "Water and wetness," 2018. Accessed: Mar. 22, 2021. [Online]. Available: https://land.copernicus.eu/pan-european/high-resolution-layers/water-wetness

[9] J. W. Jones, "Improved automated detection of subpixel-scale inundation-revised dynamic surface water extent (DSWE) partial surface water tests," *Remote Sens.*, vol. 11, no. 4, 2019, Art. no. 374.

[10] J.-F. Pekel, A. Cottam, N. Gorelick, and A. S. Belward, "High-resolution mapping of global surface water and its long-term changes," *Nature*, vol. 540, no. 7633, pp. 418–422, 2016.

[11] A. H. Pickens *et al.*, "Mapping and sampling to characterize global inland water dynamics from 1999 to 2018 with full landsat time-series," *Remote Sens. Environ.*, vol. 243, pp. 111792, 2020, Art. no. 111792.

[12] I. Klein, U. Gessner, A. J. Dietz, and C. Kuenzer, "Global waterpack—A 250 m resolution dataset revealing the daily dynamics of global inland water bodies," *Remote Sens. Environ.*, vol. 198, pp. 345–362, 2017.

[13] J. Townshend, "Global forest cover change (GFCC) water cover 2000 global 30 m V001," *NASA EOSDIS Land Processes DAAC*. Accessed: Jun. 3, 2021. [Online]. Available: https://doi.org/10.5067/MEaSUREs/GFCC/GFCC30WC.001

[14] M. Buchhorn, M. Lesiv, N.-E. Tsendbazar, M. Herold, L. Bertels, and B. Smets, "Copernicus global land cover layers-collection 2," *Remote Sens.*, vol. 12, no. 6, 2020, Art. no. 1044.

[15] K. Koppel, K. Zalite, A. Sisas, K. Voormansik, J. Praks, and M. Noorma, "Sentinel-1 for urban area monitoring-analysing local-area statistics and interferometric coherence methods for buildings' detection," in *IEEE Int. Geosci. Remote Sens. Symp*, 2015, pp. 1175–1178.

[16] D. Amitrano *et al.*, "Sentinel-1 for monitoring reservoirs: A performance analysis," *Remote Sens.*, vol. 6, no. 11, pp. 10676–10693, 2014.

[17] E. O. Makinde and O. E. Oyelade, "Land cover mapping using sentinel-1 SAR satellite imagery of Lagos state for 2017," *Proceedings*, vol. 2, no. 22, 2018, Art. no. 1399.

[18] M. R. Rahman and P. K. Thakur, "Detecting, mapping and analysing of flood water propagation using synthetic aperture radar (SAR) satellite data and GIS: A case study from the Kendrapara district of Orissa state of India," *Egyptian J. Remote Sens. Space Sci.*, vol. 21, pp. S37–S41, 2018.

[19] K. Uddin, M. A. Matin, and F. J. Meyer, "Operational flood mapping using multi-temporal Sentinel-1 SAR images: A case study from Bangladesh," *Remote Sens.*, vol. 11, no. 13, 2019, Art. no. 1581.

[20] M. Santoro and U. Wegmüller, "Multi-temporal SAR metrics applied to map water bodies," in *Proc. IEEE Int. Geosci. Remote Sens. Symp.*, 2012, pp. 5230–5233.

[21] E. Ferrentino, F. Nunziata, A. Buono, A. Urciuoli, and M. Migliaccio, "Multipolarization time series of sentinel-1 SAR imagery to analyze variations of reservoirs' water body," *IEEE J. Sel. Topics Appl. Earth Observ. Remote Sens.*, vol. 13, pp. 840–846, 2020.

[22] M. Schmitt, "Potential of large-scale inland water body mapping from Sentinel-1/2 data on the example of Bavaria's lakes and rivers," *PFG- J. Photogrammetry, Remote Sens. Geoinformat. Sci.*, vol. 88, pp. 271–289, 2020.

[23] A. Gulácsi and F. Kovács, "Sentinel-1-imagery-based high-resolution water cover detection on wetlands, aided by Google Earth Engine," *Remote Sens.*, vol. 12, no. 10, 2020, Art. no. 1614.

[24] N. Gorelick, M. Hancher, M. Dixon, S. Ilyushchenko, D. Thau, and R. Moore, "Google Earth Engine: Planetary-scale geospatial analysis for everyone," *Remote Sens. Environ.*, vol. 202, pp. 18–27, Jan. 2017.

[25] A. Vollrath, A. Mullissa, and J. Reiche, "Angular-based radiometric slope correction for Sentinel-1 on Google Earth Engine," *Remote Sens.*, vol. 12, no. 11, 2020, Art. no. 1867.

[26] W. Zhao, C.-A. Deledalle, L. Denis, H. Maître, J.-M. Nicolas, and F. Tupin, "Ratio-based multitemporal SAR images denoising: RABASAR," *IEEE Trans. Geosci. Remote Sens.*, vol. 57, no. 6, pp. 3552–3565, Jun. 2019.

[27] ESA, "Sentinel-2 Data Products," 2020, Accessed: Sep. 22, 2020. [Online]. Available: https://sentinel.esa.int/web/sentinel/missions/sentinel-2/data-products

[28] I. H. Witten, *Data Mining*. Burlington, MA, USA: Morgan Kaufmann Publisher, 2016.

[29] P. Wessel and W. H. Smith, "A global, self-consistent, hierarchical, high-resolution shoreline database," *J. Geophysical Res., Solid Earth*, vol. 101, no. B4, pp. 8741–8743, 1996.

[30] D. Small, "Flattening gamma: Radiometric terrain correction for SAR imagery," *IEEE Trans. Geosci. Remote Sens.*, vol. 49, no. 8, pp. 3081–3093, Aug. 2011.

[31] J. Takaku, T. Tadono, M. Doutsu, F. Ohgushi, and H. Kai, "Updates of 'AW3D30' ALOS global digital surface model with other open access datasets" *Remote Sens. Spatial Inf. Sci.*, vol. 43, pp. 183–189, 2020.

[32] Regione Lombardia, *Dusaf 6.0 - Uso del suolo*, 2018, Accessed: Mar. 9, 2021. [Online]. Available: https://www.dati.lombardia.it/Territorio/Dusaf-6-0-Uso-del-suolo-2018/7rae-fng6

[33] CORINE CopernicusLand Cover, 2018, Accessed: Jun. 14, 2021. [Online]. Available: https://land.copernicus.eu/pan-european/corine-land-cover

[34] WorldWater ESA, 2021. [Online]. Available: https://worldwater.earth/

David Marzi (Student Member, IEEE) received the B.Sc. degree in electronics and computer engineering in 2017 and the M.Sc. degree in electronic engineering (summa cum laude) in 2019 from University of Pavia, Pavia, Italy, where he is currently working toward the Ph.D. degree in electronic engineering.

He collaborates with an academic spin-off in Earth observation as a Radar Remote Sensing Specialist, where he is involved in developing innovative agro-tech solutions. His research focuses on analysis and fusion of multitemporal, multiresolution, and multi-frequency SAR data for vegetation mapping and monitoring.

Paolo Gamba (Fellow, IEEE) is currently a Professor with the University of Pavia, Pavia, Italy, where he leads the Telecommunications and Remote Sensing Laboratory.

Prof. Gamba was the Chair of the Data Fusion Committee of the IEEE Geoscience and Remote Sensing Society (GRSS) from October 2005 to May 2009 and the Editor-in-Chief of the IEEE Geoscience and Remote Sensing Letters from 2009 to 2013. Since 2014, he has been elected in the GRSS AdCom, the GRSS President from 2019 to 2020, and is currently GRSS Junior Past President. He was the organizer and Technical Chair of the biennial GRSS/ISPRS Joint Workshops on Remote Sensing and Data Fusion over Urban Areas from 2001 to 2015. He was also the Technical Co-Chair of the 2010, 2015, and 2020 IGARSS conferences, in Honolulu (Hawaii), Milan (Italy), and online, respectively.